Diffuse X-ray scattering from ion-irradiated materials: A parallel-computing approach

J. Channagiri, Alexandre Boulle, A. Debelle

Diffuse X-ray scattering from ion-irradiated materials:

A parallel-computing approach

J. Channagiri [a], A. Boulle [a], A. Debelle [b]

[a] Science des Procédés Céramiques et Traitements de Surfaces, CNRS UMR 7315, Centre Européen de la Céramique, 12 rue Atlantis, 87068 Limoges Cedex, France.

[b] Centre de Sciences Nucléaires et de Sciences de la Matière, Université Paris-Sud, CNRS/IN2P3, 91405 Orsay, France.

Abstract

A computational method for the evaluation of the two-dimensional diffuse X-ray scattering distribution from irradiated single crystals is presented. A Monte Carlo approach is used to generate the displacement field in the damaged crystal. This step makes use of vector programming and multi-processing to accelerate the computation. Reciprocal space maps are then computed using GPU-accelerated fast Fourier transforms. It is shown that this procedure allows to speedup the calculation by a factor ~ 190 for a crystal containing 10^9 unit-cells. The potential of the method is illustrated with two examples: the diffuse scattering from a single crystal containing (i) a non-uniform defect depth-distribution (with a potentially bi-modal defect size distribution) and, (ii) spatially correlated defects exhibiting either long-range or short-range ordering with varying positional disorder.

1. Introduction

Ion beams produced by particle accelerators are used in many fields of materials science, such as the implantation of semiconductors (Chason *et al.*, 1997) or the synthesis of nanostructured materials (Dhara, 2007). In the field of nuclear energy research, ion beams are used to simulate, in a controlled way, the different irradiation conditions to which materials will be exposed when used in fission or fusion reactors or as confinement materials for nuclear waste storage (Thomé & Garrido, 2001). Whether ion beams are used to intentionally modify the properties of materials, or to simulate their degradation under irradiation, the understanding of the fundamental effects of the interaction of high-energy particles with matter is of utmost importance.

When an energetic ion penetrates a solid, it may collide with the nuclei of the target atoms, thereby transferring part of its kinetic energy which leads the target atoms to be displaced from their equilibrium position. If the transferred kinetic energy exceeds a threshold energy (that depends on the material), the target atoms can permanently leave their position in the lattice, hence creating point defects (Frenkel pairs) which may further rearrange to form larger scale defects (point-defect cluster, dislocations loops, etc.) (Krasheninnikov & Nordlund, 2010; Becquart & Domain, 2011; Debelle *et al.*, 2014). The radiation effects are intrinsically a multi-scale phenomenon: the initial collision event occurs between two atoms but the associated damage may extend over several tens of nanometers by the formation of collision cascades and subsequent defect migration. Any experimental or computational approach to the understanding of radiation damage in materials must therefore take into account this multi-scale property of the phenomenon. For instance, molecular dynamics simulations, which consist in numerically solving the equations of motion for an ensemble of interacting particles, is ideally suited for the theoretical investigation of radiation damage: atomic scale interactions are in general described using empirical, analytical, potentials and, with the most recent developments, the simulation cells can contain up to several hundreds of millions of atoms, *i.e.* several hundreds of

nanometers in all three directions (Zarkadoula *et al.*, 2013; Nordlund & Djurabekova, 2014) which permits an almost one-to-one comparison with experimental data.

On the experimental side, X-ray diffraction (XRD) is highly sensitive to atomic scale displacements while probing macroscopic volumes, which makes it a method of choice to study radiation damage and this technique is purposely used to this end since several decades. For instance, in ion-irradiated single crystals, the analysis of the coherent scattering, using numerical simulations, allows a precise determination of the radiation-induced strain profiles and root-mean-squared lattice displacement (damage) profiles (Speriosu, 1981; Klappe & Fewster, 1994; Milita & Servidori, 1995; Boulle & Debelle, 2010). Besides these phenomenological quantities, precious information regarding, for instance, the type and the dimensions of the defects formed can be obtained by the investigation of the diffuse X-ray scattering (DXS) (Dederichs, 1971; Larson & Schmatz 1973; Ehrhart *et al.*, 1982; Nordlund *et al.*, 2000; Beck *et al.*, 2000). However, an important limitation in this approach is that tractable equations of the DXS intensity distribution can only be obtained in some relatively simple cases, say, homogeneously distributed defects, of the same type and the same size, whereas actual samples may contain defects of different types, sizes, etc. This issue can be solved by a numerical evaluation of the DXS intensity distribution, although, since we are considering the scattering from large single crystals the computation times might be prohibitive, especially if one wishes to retain (at least) the unit-cell resolution in the description of the structure of the disordered materials.

Such an approach has been suggested in pioneering studies in the early 2000s, combining atomistic simulation of the damaged crystal structure and a direct numerical evaluation of the scattered intensity (Nordlund, 2000). However, because of limitations in the computing power, the approach was restricted to relatively small crystals (a few 10^6 *atoms*) containing only a few defects. In the present work we present a powerful approach that allows to compute the two-dimensional distribution of the scattered intensity (*i.e.* reciprocal space maps, RSMs) for very large crystals (up to a few 10^9 *unit-*

cells), with realistic defect structures, in a limited amount of time. Our approach (detailed in § 3) is actually divided in two steps. In the first step a defective crystal structure is generated using a Monte Carlo evaluation procedure. In this step, high computing performances are reached by combining array (*i.e.* vector) programming and multi-processing. The second step consists in computing the RSMs, a task that is efficiently performed on a graphical processing unit (GPU) in order to reach the highest possible computing speed. We show below that our approach allows to reduce the computing time by more than two orders of magnitude. The next section (§ 2) briefly details the foundations which we rely on in this work. Selected examples will be given and discussed in § 4.

2. Theoretical background

We shall start with writing the amplitude scattered from an ensemble of unit-cells with structure factor $F(Q)$ (**Q** being the scattering vector):

$$A(\mathbf{Q}) = \sum_j F_j(Q) \exp\left[i\,\mathbf{Q}\left(\mathbf{r}_j + \mathbf{u}_j\right)\right] \quad , \tag{1}$$

where $\mathbf{r}_j$ is the position of the j^{th} unit-cell in the ideal structure, and $\mathbf{u}_j$ is its displacement from the ideal structure. In the limit of small displacements we can make the common assumption that $\mathbf{Q}\,\mathbf{u} \approx \mathbf{H}\,\mathbf{u}$ (where **H** is the reciprocal lattice vector of the reflection considered) so that the amplitude can be written

$$A(\mathbf{Q}) = F_O(Q)\,\mathrm{FT}\left[V(\mathbf{r}_j) G(\mathbf{r}_j)\right] \quad , \tag{2}$$

where we introduced the crystal shape function $V(\mathbf{r})$ which is equal to one when the position vector **r** points inside the crystal, and 0 otherwise. $G(\mathbf{r})$ is the correlation function

$$G(\mathbf{r}) = \bar{\rho}(\mathbf{r}) \exp\left[i\,\mathbf{H}\,\mathbf{u}(\mathbf{r})\right] \quad , \tag{3}$$

where the relative scattering density is written

$$\bar{\rho}(\mathbf{r}) = 1 + \frac{\Delta F(\mathbf{r})}{F_0} \quad . \tag{4}$$

The relative scattering density allows to take into account the fact that the structure factor of a unit-cell containing a defect, F_{defect}, may defer from the ideal structure factor, *i.e.* $F_{\text{defect}} = F_0 + \Delta F$. For instance, in the case of porous regions (*i.e.* vacancy clusters), $\bar{\rho}(\mathbf{r}) = 0$. If the displacement field $\mathbf{u}(\mathbf{r})$ is known, then the intensity can be straightforwardly computed from equations (2-4) and $|A(\mathbf{Q})|^2$.

In an actual experiment, the intensity recorded on the detector results from the incoherent superposition of the intensities diffracted by different regions of the crystal, so that the quantity that should be computed is $\langle|A(\mathbf{Q})|^2\rangle$ where the average is performed over the different regions of the crystal, *i.e.* over different defect configurations. This lack of coherence may result from the fact that the beam coherence length is larger that the coherently-diffracting domain size of the sample, or that the beam coherence length is smaller than the actual dimension of the beam, hence resulting in a (partially) incoherent illumination of the sample. Besides, on laboratory experiments the beam is often only poorly collimated in the direction normal to the scattering plane (the plane defined by the incident and diffracted beam), resulting in axial divergences of the order of a few degrees, so that the diffracted intensity can be (infinitely) integrated over Q_y (Kaganer *et al.*, 1997; Boulle *et al.*, 2006a):

$$\left\langle I(Q_x, Q_z)\right\rangle = \int dQ_y \cdot I(\mathbf{Q}) \tag{5}$$

where Q_y is the component of the scattering vector normal to the scattering plane, Fig. 1(a). Let us develop the intensity on the right hand side of equation (5):

$$\begin{aligned} I(\mathbf{Q}) = |F_0|^2 \sum_{p,p'} \sum_{q,q'} \sum_{r,r'} & G(x_p, y_q, z_r) G^*(x_{p'}, y_{q'}, z_{r'}) \\ & \times \exp\left[iQ_x(x_p - x_{p'})\right] \exp\left[iQ_y(y_q - y_{q'})\right] \exp\left[iQ_z(z_r - z_{r'})\right] \end{aligned} \tag{6}$$

Equation (5) can hence be rewritten :

$$\begin{aligned} I(\mathbf{Q}) = |F_0|^2 \sum_{p,p'} \sum_{q,q'} \sum_{r,r'} & G(x_p, y_q, z_r) G^*(x_{p'}, y_{q'}, z_{r'}) \\ & \times \exp\left[iQ_x(x_p - x_{p'})\right] \exp\left[iQ_z(z_r - z_{r'})\right] \int dQ_y \cdot \exp\left[iQ_y(y_q - y_{q'})\right] \end{aligned} \tag{7}$$

The integral term in equation (7) is the delta function $\delta(y_q, y_{q'})$ and is hence equal to one for $y_q = y_{q'}$ (and equal to zero elsewhere). The averaged intensity finally reads

$$\langle I(Q_x, Q_z)\rangle = \sum_q |F_0|^2 \sum_{p,p'} \sum_{r,r'} G(x_p, y_q, z_r) G^*(x_{p'}, y_q, z_{r'}) \times \exp\left[i Q_x \left(x_p - x_{p'}\right)\right] \exp\left[i Q_z \left(z_r - z_{r'}\right)\right] \quad . \tag{8}$$

The previous equation can be written in condensed form

$$\langle I(Q_x, Q_z)\rangle = \sum_q |F_0|^2 |\mathrm{FT}\left[V_q(x, z) G_q(x, z)\right]|^2 \quad , \tag{9}$$

where the two-dimensional correlation function $G_q(x, z)$ is

$$G_q(x, z) = \bar{\rho}(x, z) \exp\left[i \mathbf{H} \mathbf{u}_q(x, z)\right] \quad . \tag{10}$$

where $\mathbf{u}_q$ is the displacement field within the q^{th} plane of the crystal. Equation (9) shows that in the diffraction experiment the crystal can be viewed as divided into unit-cell – thick (x, z) planes, parallel the scattering plane, that diffract incoherently with each other, as schematically represented in Fig. 1(a). The intensity diffracted from each (x, z) plane is given by the squared modulus of the amplitude scattered from each plane, and the intensities are summed up to form the total scattered intensity. In the next section we show how equations (9-10) can be efficiently implemented to compute the scattering from defective crystals, with a special interest for irradiated single crystals.

It should be stressed that the approach presented below assumes the validity of the above-mentioned assumption stating that $\mathbf{Q}\,\mathbf{u} \approx \mathbf{H}\,\mathbf{u}$, which allows to make use of Fourier transformation. Therefore, for large deviations from the scattering vector from the center of the Bragg reflection, combined with large lattice displacements (like dislocation cores for instance), the previous assumption obviously does not hold. In such cases, only the scattering in the close vicinity of the Bragg peak should be considered.

3. Implementation

3.1. Computational details

All computations have been performed on a desktop workstation equipped with two Intel Xeon E5-2609 (4 cores, 2.5 GHz clock frequency) central processing units (CPUs), 64 GB of RAM and a Nvidia

Quadro K4000 GPU (3GB memory, 768 CUDA cores, with compute capability 3.0).

We used the Python programming language (https://www.python.org/) together with the NumPy (http://www.numpy.org/) and SciPy (http://www.scipy.org/) libraries in order to benefit from vector programming capabilities and extended mathematic and scientific functions (Oliphant, 2007). Python natively supports parallel computing through the dedicated `multiprocessing` module. The implementation on the GPU uses Nvidia's CUDA (Compute Unified Device Architecture) application programming interface through the python pyCUDA wrapper (Klöckner *et al.*, 2012 ; http://mathema.tician.de/software/pycuda/). GPU-based fast Fourier transformations were performed using the pyFFT module (https://pythonhosted.org/pyfft/). Although GPU-based computing is a relatively new field, we will not discuss here its relevance and limitations in the field of X-ray crystallography as this topic has been covered in details previously, in the past five years in the present Journal (Gutmann, 2010; Gelisio *et al.*, 2010; Favre-Nicolin *et al.*, 2011; Shalaby & Oliveira, 2013).

3.2. The displacement field

In the framework of linear elasticity, the displacement at a given point **r** in the crystal results from the superposition of the displacement fields of all defects in the crystal (Krivoglaz, 1969):

$$\mathbf{u}(\mathbf{r}) = \sum_{\alpha,j} c_{\alpha,j}\,\mathbf{u}_{\alpha,j}(\mathbf{r}-\mathbf{r}_j) \tag{11}$$

where $c_{\alpha,j}$ is the probability of having a defect of type α at the j^{th} lattice site, and $\mathbf{u}_\alpha(\mathbf{r})$ is the corresponding displacement field. As mentioned above, irradiation gives rise to point defects which may migrate to form mostly spherical point-defect clusters. For simplicity, in the present article, we shall focus on spherical defects, although the approach detailed here is by no means restricted to spherical defects and can be used for any type of defect of any shape, as long as the corresponding displacement field can be computed.

The displacement field associated to a spherical defect with radius R_α can be written, assuming an

elastically isotropic crystal (Pietsch *et al.*, 2004):

$$\mathbf{u}_\alpha(\Delta\mathbf{r}) = \begin{cases} A\Delta\mathbf{r}/R_\alpha^3 & \text{if } |\Delta r| \le R_\alpha \\ A\Delta\mathbf{r}/\Delta r^3 & \text{if } |\Delta r| > R_\alpha \end{cases} \tag{12}$$

where $A = \varepsilon\ R_\alpha^3\ (1 + \nu) / [3(1 - \nu)]$ (ε being the lattice mismatch between the defect and the ideal crystal and ν is the Poisson's ratio of the crystal).

We suggest to evaluate equation (11) numerically using a Monte Carlo summation procedure[1]. For this purpose, we generate a three-dimensional NumPy array containing N unit-cells, and defect coordinates $\mathbf{r}_j$ are randomly chosen within this array. The displacement field corresponding to each defect $\mathbf{u}_\alpha$ is computed with equation (11) and added to the total displacement field $\mathbf{u}$. This procedure is repeated until the maximum number of defects $N<c_\alpha>$ is reached. The most interesting feature in this approach is that the defect locations can be tuned in order to match the actual defect structure of the samples investigated, *i.e.* the defect distribution is not restricted to a random distribution. Spatially correlated defects, defect interactions (with a variable attraction or repelling zone), concentration gradients, etc., can be straightforwardly implemented in this approach. Examples will be given in the next section.

The obvious drawback of the approach is the time and memory needed to compute equation (11). For instance, a crystal with $N = 10^9$ unit-cells and displacement values coded over 64 bits (double-precision floating-point numbers) requires 8 GB memory. Since two copies of the displacement field has to be stored in the memory during the computation (corresponding to the total $\mathbf{u}$ and the current $\mathbf{u}_\alpha$ displacement field) the total memory needed to compute equation (11) reaches 16 GB. Our current GPU is limited to 3GB, but even the best and most recent GPU available to date are limited to 12 GB memory which unfortunately prohibits their use for this calculation. Additionally, it is worth emphasizing that, given the large amount of data to transfer to the GPU as compared to the very small computational cost of equation 11 (one array addition per computed $\mathbf{u}_\alpha$), the acceleration would

1 The Monte Carlo procedure is here used to generate a static three-dimensional displacement field assuming some predefined defect characteristics (defect radius, misfit, etc.). It does not allow to describe the evolution of the microstructure under the action of external stimuli (temperature, irradiation, etc.), which constitutes a topic by itself.

certainly not be very favorable. Moreover, the computation pathway cannot be determined in advance since the selection of random coordinates inside the three-dimensional NumPy array heavily relies on conditional instructions (`if`, `then`, `else`), for instance to produce non-random defect distributions, which is not ideal for the implementation on the GPU (Favre-Nicolin *et al.*, 2011).

In order to keep the memory footprint as low as possible and to maximize the computing speed the evaluation of equation (12) has been implemented in C language and integrated in the python code using the `weave` module of the SciPy library. Despite this procedure, for $N = 10^9$ unit-cells, the computation still requires a few seconds, which is prohibitive, especially if several thousands of defects have to be generated. To circumvent this issue, we make use of a specific feature of the NumPy arrays known as "slicing" (van de Walt, 2011): once an array is created it is possible to extract any sub-part (a "view") of the array with no need to copy to the memory and at no computational cost (generating a view is performed in a few tens of microseconds). We hence generate a template displacement field for a crystal with twice the dimensions of the actual crystal in all directions, containing a defect in its center. A two-dimensional schematic is given in Fig. 1(b). From this template, any displacement field corresponding to the actual crystal, can be extracted using $\mathbf{u}_\alpha(\Delta\mathbf{r}) = \mathbf{u}_{\text{template}}(\mathbf{D} - \mathbf{r}_j + \Delta\mathbf{r})$, where $\mathbf{D} = (D_x, D_y, D_z)^T$ is the size of the array. Equation (11) is then computed using the vectorized addition of the NumPy arrays. It should be noted that this approach assumes that the displacement field around the defect is identical for all defects, independently of their location within the crystal. In particular this excludes the influence of free surfaces. In the case of sufficiently large crystals this effect is probably not dominant, but this approach could clearly not be used in the case of nanostructures.

The speedup obtained for the computation of the displacement field with this approach (as compared to the direct computation of equation 12) is displayed in Fig. 2(a) for increasing crystal size, with a fixed defect density $\langle c_\alpha \rangle = 10^{-5}$ defects/unit-cell. For arrays with less than 10^6 unit-cells there is no real gain in using the template-slicing approach; this finding likely stems from the fact that the time needed to

create the template compensates the gain obtained by generating a view of it. For larger arrays, the speedup steadily increases, reaching a value of ~15 for $N = 10^9$ unit-cells.

An intrinsic limitation when working with large data sets comes from the time needed to transfer the data from the memory to the CPU; this issue can in principle be solved by GPU computing (Schmeisser *et al.*, 2009) provided that the amount of GPU memory is sufficient, though. In the present case, we propose to side-step this problem using multi-processing, *i.e.* the calculation of the displacement field is distributed over the different cores of the processor. The parallelization can be performed in several ways; here we have chosen to parallelize over the dimension of the crystal in the *y*-direction, so that each process computes the displacement field in a sub-region of the crystal. At the end of the calculation the different sub-regions are combined to form the entire displacement field. The main advantage of this approach, besides the obvious increased computing power, is that each process deals with a smaller array, hence resulting in increased transfer speed from memory to CPU. The corresponding speedup for increasing crystal size is displayed in Fig. 2(b). For crystal sizes smaller than $N = 10^7$ unit-cells, the speed-up increases steadily and, as expected, the computing speed obtained with 8 processors is, respectively, 2 and 4 times faster than the speed obtained with 4 and 2 processors. Above 10^7 unit-cells, whereas the slope of the curve corresponding to 2 processors remains unchanged, the speedup obtained with 8 processors considerably increases (eventually saturating at a value of 22.5 for $N>5\times10^8$ unit-cells, *vs.* 3.1 for 2 processors). This behavior can probably be attributed to the fact that for those larger arrays, the speedup is limited by the time needed to transfer the data, an effect which is less pronounced when dealing with smaller arrays, hence the increased speedup when using multiple processors. It should be noted that, for this last benchmark, the time measurements (including the reference time with only one processor) include the template-slicing modification detailed above. The total speedup therefore correspond to the product of both curves; in the best case we reach a total speedup of $22.5\times15 = 337.5$.

3.3. The scattered intensity

We now focus on the evaluation of the scattered intensity. Equation (9) shows that it is actually the sum of (the squared modulus of) two-dimensional Fourier transforms that can be evaluated independently. We here propose to compute the Fourier transform on the GPU using a fast Fourier transform (FFT) algorithm. The computational cost of FFT algorithms scales as $N \log(N)$ (N points in real space, N points in reciprocal space spanning a complete reciprocal unit-cell), *versus* N^2 for a direct evaluation of the sum, which makes FFTs particularly relevant for the large crystal sizes considered in this work. Therefore, even if only a small fraction of the computed RSM is required, it is still considerably interesting to use an FFT algorithm.

With an input array of size D'_i in a given direction, the FFT returns an array with spacing $1/D'_i$ in the associated direction. The size of the input array has therefore to be adjusted according to the desired reciprocal space resolution. A rule of thumb is that if the crystal size is D_i in a given direction, then the tiniest (finite size) interference feature will exhibit a period of $1/D_i$. Basic oversampling considerations requires an oversampling factor of two (the Nyquist rate). Here, in order to correctly describe an interference fringe without impairing the computation time, we chose an oversampling rate of 4, so that we obtain the condition $D'_i = 4 \times D_i$ (with $i = x, z$). In the y-direction the summation is incoherent so that we can take $D'_y = D_y$.

In equation (9) the shape and size of the crystal are described by the term $V_q(x, z)$. In the present work we restricted the study to parallelepipedic shapes such that $V_q(x, z) = V(x)V(z)$ and we wrote

$$V(i) = \frac{1}{2}\left[1 - erf\left(\frac{i - D_i}{\sqrt{2}\,\sigma_i}\right)\right] \tag{13}$$

where $i = x, z$. Equation (13) allows, if needed, to account for fluctuations of the crystal size. For simplicity, the size distribution is assumed to be Gaussian, with standard deviation σ_i. The presence of

size fluctuations smears out the size-induced interference fringes as detailed elsewhere (Boulle *et al.*, 2006a, 2006b). When $\sigma_i \rightarrow 0$, equation (13) is a top-hat function (= 1 if $0 \leq x \leq D_i$, 0 otherwise) and its FFT is equal to a sinc function with well defined interference fringes with period $1/D_i$.

Equations (9) and (10) are directly evaluated on the GPU after the two-dimensional view $\mathbf{u}_q(x,z)$ has been extracted from the three-dimensional displacement field $\mathbf{u}(\mathbf{r})$ computed in the previous section, and this operation is repeated for all values of q, *i.e.* all (x, z) planes in the crystal. The speedup obtained using the GPU instead of a classical CPU evaluation is displayed in Fig. 1(c). As expected, the speedup is mainly relevant for large array sizes, with a maximum efficiency (speedup = 45) reached at $N = 10^6$ unit-cells.

The total speedup obtained with our approach has been evaluated with the following example: the computation of the 004 reflection of a crystal with 1000×1000×1000 unit-cells (with a 5 Å lattice parameter and $\nu = 0.3$) containing 10^4 defects (*i.e.* $\langle c_1 \rangle = 10^{-5}$ defects / unit-cell) with radius $R_1 = 5$ nm and 5% lattice mismatch. The calculation lasted 26 minutes using our optimized approach (11 minutes to generate the displacement field, 15 minutes to compute the RSM), versus 83 hours using a non-parallel approach, *i.e.* a total speedup of 191. Obviously, the scattering from randomly distributed spherical defects can be computed in a few seconds using the appropriate analytical expressions (Pietsch *et al.*, 2004). Our approach reveals all its potential when dealing with more complex defect distributions for which analytical solutions are hardly obtainable. This will be the topic of the next section.

As mentioned earlier, the integration along the y direction leads to an incoherent addition of the intensities scattered from the different (x, z) planes. The choice of the crystal dimension in this direction hence does not affect the shape the scattered intensity and can be used to adjust the computing times. It must, however, be borne in mind that higher values of D_y will improve the signal/noise ratio of

the computed RSMs. Indeed, the FFT of a single (x, z) plane exhibits a complex fringes pattern (a speckle pattern) corresponding to the scattering from a given defect configuration. The summation over different planes along y smears out these patterns and produces the configuration-averaged signal, as measured experimentally. This situation is illustrated in Fig. 3 where we plot h-scans (extracted at $\Delta\underline{l} = -0.12$) corresponding to the previous example (gray dots). It can be readily observed that increasing the number of lattice planes in the y direction allows to reduce the level of noise in the computed curves, while the overall shape of the curves remain unchanged. This can be quantified by computing the root-mean-squared (rms) deviation of the scattered intensity σ_I (see equation (14) in Kaganer & Sabefeld, 2009). In this example, the maximum rms deviation (relative to the diffracted intensity, σ_I / I) ranges from 25% when only 10 lattice planes are used, to 0.2% for 1000 lattice planes. A smooth curve (with rms deviation of 0.4%) is obtained for 500 lattice planes.

The quality of the computed curves can be dramatically increased, while reducing the computing times, by convolving the computed curves with a blurring function. Experimentally, this corresponds to the resolution function of the diffractometer (which reflects the coherence properties of the beam), and which can be obtained either by the measurement of a perfect reference crystal, or calculated by taking into account the different elements in the beam path (Boulle *et al.*, 2002). Eventually, this procedure should allow to quantitatively compare (fit) the computed curves with experimental data. In the present article we do not consider quantitative fitting of data and the resolution function is simply assumed to be a two-dimensional Gaussian with a full-width at half-maximum of 2×10^{-4} Å in both directions of reciprocal space (which corresponds to an isotropic spatial coherence length of ~ 3 μm). Fig. 3 shows that this procedure allows to obtain relatively smooth data from ~100 lattice planes (*i.e.* 5 times less than without convolution). Additionally, this procedure allows to clearly resolve tiny features in the curves, such as the narrow coherent Bragg peak located at $\Delta h = 0$, in situations where they are completely masked by the noise when no convolution is used.

4. Application to irradiated single crystals

4.1. Non-uniform and bimodal defect distribution

For this example, we shall consider the case of yttria-stabilized zirconia (YSZ) single crystals, whose behavior under different irradiation conditions is well documented (Debelle *et al.*, 2014; Moll *et al.*, 2009; Vincent *et al.*, 2008, Yang *et al.*, 2013). In these materials, the damage build-up upon increasing ion fluence takes place by a multi-step process, each step occurring in order to lower the system's free energy. In the first step, point-defects, mainly Frenkel pairs, are formed[2] in a sub-surface region whose extension varies from ~100 nm to a few hundreds of nanometers, depending on the nature and energy of the incident ions (the defect distribution in the damaged region being non-uniform). In the next steps, these point defects coalesce to form larger (a few nanometers) point-defect clusters and, ultimately, an intricate network of dislocation loops. The defect mobility can be increased by performing irradiation at high temperature which results in a shift of the different steps towards lower fluences, *i.e.* the increased defect mobility favors defect clustering at lower fluences.

The microstructure of those irradiated YSZ single crystals has been modeled as follows. Defects are randomly created in the crystal according to an arbitrary density function corresponding to the probability to observe a defect at a given depth below the surface, Fig. 4(a). The shape of the density function has been chosen so as to be similar to disorder profiles determined by ion channeling and X-ray diffraction (Debelle *et al.*, 2014) in actual irradiated crystals. In a first step, unit-cell – sized defects are created (R_1 = 5 Å, ε = 5%) with concentration $\langle c_1 \rangle$ = 0.01 defect/unit-cell. A section of the computed two-dimensional strain field is shown in Fig. 4(b). It can be seen that the defects produce tensile strain (white regions) in the 0-200 unit-cells range below the surface. For depths larger than 200

2 In these fluorite-type structure the most stable defect appears to be a Frenkel pair, where a cation leaves its ideal site to occupy the center of the oxygen cube in the center of the unit-cell (Van Brutzel *et al.*, 2008). The corresponding fractional displacement is 0.5, so that the structure factor of the 004 reflection is not affected. Therefore, ΔF was set to 0 in the calculations.

unit-cells, no tensile strain can be detected.

The corresponding 004 RSM is shown in Fig. 5(a) and selected scans are displayed in Fig. 5(d, e). The RSM exhibits an elongated streak parallel to the *l* direction, with the Bragg peak (emanating from the virgin part of the crystal) located at $\Delta l = 0$ and a secondary maximum located at $\Delta l = -0.04$. This signal is typical of irradiated materials exhibiting a dilatation gradient in the direction perpendicular to the surface (Boulle & Debelle, 2010). This result shows that a dilatation (*i.e.* homogeneous strain) gradient can be produced in irradiated crystals with a non-uniform distribution of unit-cell – sized defects. In addition, it can be seen that the DXS is extremely weak and drops rapidly down to values 10^5 times lower than the coherent signal , *i.e.* the intensity is mainly concentrated within the damage-induced streak. It can also be noticed that, in addition to the vertical streak, a horizontal streak is also observed at $\Delta l = 0$. This feature corresponds to the crystal truncation rods (CTR) and is due to the finite dimensions of the crystal used in the calculation. This latter streak is in general not observed in the scattering from single crystals as the dimensions of actual coherent domains are larger than the dimensions considered here (500 unit-cells).

In a second step, we generated a structure where 25% of the initial defects were allowed to coalesce to form larger defects with $R_2 = 5$ nm. The corresponding RSM is given in Fig. 5(b). The intensity of the damage-induced streak is lowered and, concomitantly the DXS intensity considerably increases (as revealed by the spreading of the intensity in the *h* direction). This feature shows that, whereas small defects are efficient in producing homogeneous strain within the damaged region of the crystal, large defects mostly give rise to heterogeneous strain. Finally, in the last step, only large defects remain, and the trend observed previously continues, Fig. 5(c). The damage-induced streak is now reduced to a weak peak on the lower *l* side of the main Bragg peak, and the DXS forms an intense, elliptically shaped halo around the Bragg peak. These features are in remarkable qualitative agreement with the tendency observed in YSZ; see for instance Fig. 5 in Debelle *et al.* (2014). In this figure, the three

different steps correspond to the irradiation performed at increasing temperatures, resulting in an enhanced defect clustering, and hence to the formation of larger defects at higher temperatures.

4.2 Spatially correlated defects

An interesting feature in the irradiation of materials is the spontaneous formation of ordered nanostructures, which is mainly observed in fcc and bcc metals. These nanostructures include, among others, self-organized three-dimensional superstructures of voids (vacancy clusters), gas bubbles or dislocations loops with varying degree of disorder (see Ghoniem *et al.*, 2002 and references therein).

In this section we investigate the effects of spatially correlated defects, in the case of long-range order (LRO) and short-range order (SRO) spatial correlations and with a varying degree of disorder. For simplicity we assumed a cubic ordering, but any type of array can be straightforwardly implemented. Additionally in order not to overly complicate the RSMs we only consider the effect of ordering of defects of the same size and we do not take into account the previous depth gradient. It must emphasized, however, that any constraint on the defect positions or defect sizes can be easily implemented without any additional computational cost. For the sake of modeling spatial correlation we use the following probability density function

$$p(x)=\sum_{n} g(x)*\delta(x-n\,\Lambda) \tag{14}$$

which corresponds to the probability of finding a defect at a distance x from another defect, Λ being the period of the superstructure. The function $g(x)$ describes the positional probability density function at each node of the superstructure. In the case of LRO it was assumed to be a Gaussian with a fixed standard deviation, σ_0, whereas in the case of SRO, the standard deviation was assumed to vary in a random-walk type fashion, $\sigma_n = n^{1/2}\,\sigma_0$ (Schmidbauer, 2004). The corresponding density functions, with Λ = 20 unit-cells, are plotted in Fig. 6 in the case of a low ($\sigma_0 = \Lambda / 12$) and a high ($\sigma_0 = \Lambda / 4$) positional disorder. Increasing the standard deviation widens the peaks of the probability density

function resulting in an increased disordering (*i.e.* the probability to find a defects never drops down to 0). In the case of SRO, this eventually leads to correlations restricted to the first neighbor.

The computed RSMs (with defect radius R_1 = 2.5 nm, *i.e.* 5 unit-cells, and ε = 5%) corresponding to each case are displayed in Fig. 7 and 8. We first discuss the case of LRO (Fig. 7). In the case of low positional disorder (Fig. 7a), the DXS is elliptically shaped with clearly visible superstructure peaks occurring for Δh, $\Delta l = n / \Lambda = n \times 0.05$ (n being an integer). The superstructure peaks occur along the coherent CTR (Fig. 7c) but also in the DXS (Fig. 7d). The intensity of the superstructure peaks is modulated by a Debye-Waller – like factor, $\exp(-2\pi^2 n^2 \sigma_0^2)$, so that for low disorder superstructure peaks are visible up to high orders n. On the contrary, as shown in Fig. 7b and in the scans Fig 7c and 7d, for increased disorder only the first order peaks are visible, and the diffuse scattering has a structured shape corresponding to the DXS from isolated defects, where the RSM exhibits two asymmetrical lobes and fringes on each side of a nodal plane located at $\Delta l = 0$ (Pietsch *et al.*, 2004). The broad secondary maximum located at $\Delta l \approx -0.12$ corresponds to the diffraction from the core of the defects. The peak shift is due to the strain inside the defect which gives rise to the observed shift of $- l \times \varepsilon \times (1 + \nu) / [3(1 - \nu)] = -0.124$ (with $\nu = 0.3$).

The case of SRO is displayed in Fig. 8. It can be readily observed that SRO leads to much less pronounced superstructure features. This can be explained by the fact that, in the case of a random walk model, the width of the superstructure peaks scales as $n^2\sigma_0^2$ (Schmidbauer, 2004), so that high order peaks are smeared out, even for relatively small values of σ_0. Therefore, for SRO, the low disorder case is similar to the high disorder case of LRO, in particular regarding the overall shape of the DXS. A closer inspection, however, reveals that the width of the first order peak is larger in the case of SRO than in LRO, in agreement with the previous statement. For higher disorder, although first neighbor correlations are present, no particular features can be detected in the RSM which correspond to the RSM from isolated point defects.

5. Discussion and conclusions

We have presented a computational method for the evaluation of the displacement field induced by defects in irradiated materials and the corresponding XRD reciprocal space maps. The total displacement field of the damaged crystals is calculated using a Monte Carlo method where the displacement fields of individual defects are summed (several defect distributions were tested). This step combines vector programming and multi-processing to speedup the calculation. The RSMs are obtained from the incoherent sum of Fourier transforms of two-dimensional slices of the correlation function. This part is computed on the GPU making use of optimized FFT algorithms. We used this approach to successfully model the DXS of irradiated zirconia single crystals containing a non-uniform defect depth-distribution and undergoing defect clustering. We showed that the proposed approach allows to qualitatively reproduce the main features observed in actual RSMs recorded from such crystals.

We believe that our approach is not limited to the study of irradiated crystals and can be used for a broad range of systems, as long as the displacement field of the defects can be computed. For instance, dislocations in thin films are the subject of thorough studies using DXS and Monte Carlo simulations (Kaganer & Sabefeld, 2009; Lazarev *et al.*, 2013) and could probably benefit from this approach (in the limits of the validity of the assumption $\mathbf{Q}\,\mathbf{u} \approx \mathbf{H}\,\mathbf{u}$, as mentioned in Sec. 2).

Future developments of this work will use the results of atomistic simulations (*i.e.* molecular dynamics) or finite-element modeling to compute the displacement field of the damaged crystals. Indeed, for very high defect concentrations, the relevance of the use of the displacement field from individual (isolated) defects to compute the total displacement field can probably be questioned. Additionally, for high defect concentrations the computation times of the displacement field become prohibitively long, even with the improvements presented in this work, so that an alternate method is preferable.

On the contrary, the GPU-accelerated approach to compute the RSMs from the displacement field is solely dependent on the crystal size, and its efficiency is independent of the complexity of the displacement field. It can hence be straightforwardly combined with any computational method that allows to compute the displacement field. Moreover, the fast-growing computing power of the GPUs will allow to study crystals with increased dimensions in the very near future.

Acknowledgements

J.C. is grateful to Région Limousin (France) for funding the Ph. D. thesis. J. C. is also thankful to Mr. A. Klöckner, Mr. B. Opanchuk and Mr. J. Kieffer for fruitful discussions related to the implementation of GPU computing. This work was partially funded by the NEEDS-Matériaux program.

References

Beck, U., Metzger, T. H., Peisl, J., Patel, J. R. (2000). *Appl. Phys. Lett.* **76**, 2698-2700.

Becquart, C. S., Domain, C. (2011). *Metall. Mater Trans. A* 42A, 852-870.

Boulle, A., Masson, O., Guinebretière, R., Lecomte, A., Dauger, A. (2002) *J. Appl. Cryst.* **35**, 606-614.

Boulle, A., Conchon, F., Guinebretière, R. (2006a) *Acta Cryst. A* **62**, 11-20.

Boulle, A., Guinebretiere, R, Masson, O., Bachelet, R., Conchon, F., Dauger, A. (2006b). *Appl. Surf. Sci.* **253**, 95-105.

Boulle, A., Debelle, A. (2010). *J. Appl. Cryst.* **43**, 1046-1052.

Chason, E., Picraux, S. T., Poate, J. M., Borland, J. O., Current, M. I., Diaz de la Rubia, T., Eaglesham, D. J., Holland, O. W., Law, M. E., Magee, C. W., Mayer, J. W., Melngailis, J., Tasch, A. F. (1997). *J. Appl. Phys.* **81**, 6513-6561.

Debelle, A., Channagiri, J., Thomé, L., Décamps, B., Boulle, A., Moll, S., Garrido, F., Behar, M., Jagielski, J. (2014). *J. Appl. Phys.* **115**, 183504 1-9.

Dederichs, P. H. (1971). *Phys. Rev. B* **4**, 1041-1050.

Dhara, S. (2007). *Crit. Rev. Sol. State Mater. Sci.* **32**, 1-5.

Ehrhart, P., Trinkaus, H., Larson, B. C. (1982). *Phys. Rev. B* **25**, 834-848.

Favre-Nicolin, V., Coraux, J., Richard, M. I., Renevier, H. (2011). *J. Appl. Cryst.* **44**, 635-640.

Gelisio, L., Ricardo C. L. A., Leoni, M., Scardi, P. (2010). *J. Appl. Cryst.* **43**, 647-653.

Ghoniem, N. M., Walgraef, D., Zinkle, S. J. (2002). *J. Comp. Aided Mater. Design* **8**, 1-38.

Gutmann, M. J. (2010). *J. Appl. Cryst.* **43**, 250-255.

Kaganer, V. M., Köhler, R., Schmidbauer, M., Opitz, R., Jenichen, B. (1997). *Phys. Rev. B* **55**, 1793-1810.

Kaganer, V. M., Sabefeld, K. K. (2009). *Phys. Rev. B* **80**, 184105 1-13.

Klappe, J. G. E. & Fewster, P. F. (1994). *J. Appl. Cryst.* **27**, 103-110.

Klöckner, A., Pinto, N., Lee, Y., Catanzaro, B., Ivanov, P., Fasih, A. (2012). *Parall. Comp.* **3**, 157-174.

Krasheninnikov, A. V., Nordlund, K. (2010). *J. Appl. Phys.* 071301 1-70.

Krivoglaz, M. A. (1969). *Theory of X-ray and Thermal Neutron Scattering by Real Crystals*. New York: Plenum.

Larson, B. C., Schmatz, W. (1974). *Phys. Rev. B* **10**, 2307-2314.

Lazarev, S., Barchuk, M., Bauer, S., Forghani, K., Holý, V., Scholz, F., Baumbach, T. (2013). *J. Appl. Cryst.* **46**, 120-127.

Milita, S. & Servidori, M. (1995). *J. Appl. Cryst.* **28**, 666–672.

Moll, S., Thomé, L., Sattonnay, G., Debelle, A., Garrido, F., Vincent, L., Jagielski, J. (2009). *J. Appl. Phys.* **106**, 073509 1-9.

Nordlund, K., Partyka, P., Averback, R. S., Robinson, I. K., Erhahrt, P. (2000). *J. Appl. Phys.* **88**, 2278-2288.

Nordlund, K., Djurabekova, F. (2014). *J. Comput. Electron* **13**, 122-141.

Oliphant, T. E. (2007). *Comput. Sci. Eng.* **9**, 10-20.

Pietsch, U., Holý, V., Baumbach, T. (2004). *High-Resolution X-ray Scattering – From Thin Films to Lateral Nanostructures*. New York: Springer-Verlag.

Schmeisser, M., Heisen, B. C., Luettich, M., Busche, B., Hauer, F., Koske, T., Knauber, K. -H., Stark, H. (2009). *Acta Cryst. D* **65**, 659-671.

Schmidbauer, M. (2004). *X-ray diffuse scattering from self-organized mesoscopic semiconductor structures*, Springer-Verlag Berlin Heidelberg.

Shalaby, E. M., Oliveira, M. A. (2013). *J. Appl. Cryst.* **46**, 594-600.

Speriosu, V. S. (1981). *J. Appl. Phys.* **52**, 6094-6103.

Thomé, L., Garrido, F. (2001). *Vacuum* **63**, 619-626.

Van Brutzel, L., Chartier, A., Crocombette, J. P. (2008). *Phys. Rev. B* **78**, 024111 1-7.

Vincent, L., Thomé, L., Garrido, F., Kaitasov, O., Houdelier, F. (2008). *J. Appl. Phys.* **104**, 114904 1-8.

van de Walt, S., Colbert, S. C., Varoquaux, G. (2011). *Comput. Sci. Eng.* **13**, 22-30.

Yang, T., Taylor, C. A., Kong, S., Wang, C., Zhang, Y., Huang, X., Xue, J., Yana, S., Wang, Y. (2013). *J. Nucl. Mater.* **443** 40-48.

Zarkadoula, E., Daraszewicz, S. L., Duffy, D. M., Seaton, M. A., Todorov, I. T., Nordlund, K., Dove, M. T., Trachenko, K. (2013). *J. Phys.: Condens. Matter* **25**, 125402 1-7.

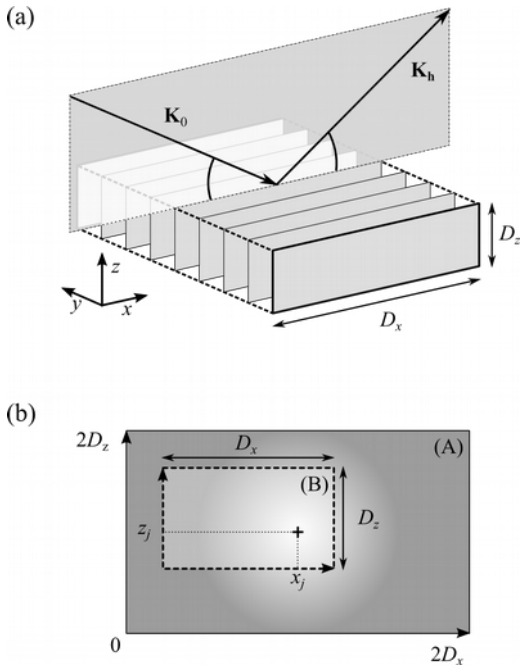

Figure 1.

(a) schematic view of the diffraction geometry. $\mathbf{K}_o$ and $\mathbf{K}_h$ are the incident and diffracted wave-vectors respectively. D_x and D_z are the dimensions of the crystal along the x and z directions, respectively.

(b) schematic representation of the template-slicing approach. The template is indicated by rectangle (A), and the extracted view by rectangle (B).

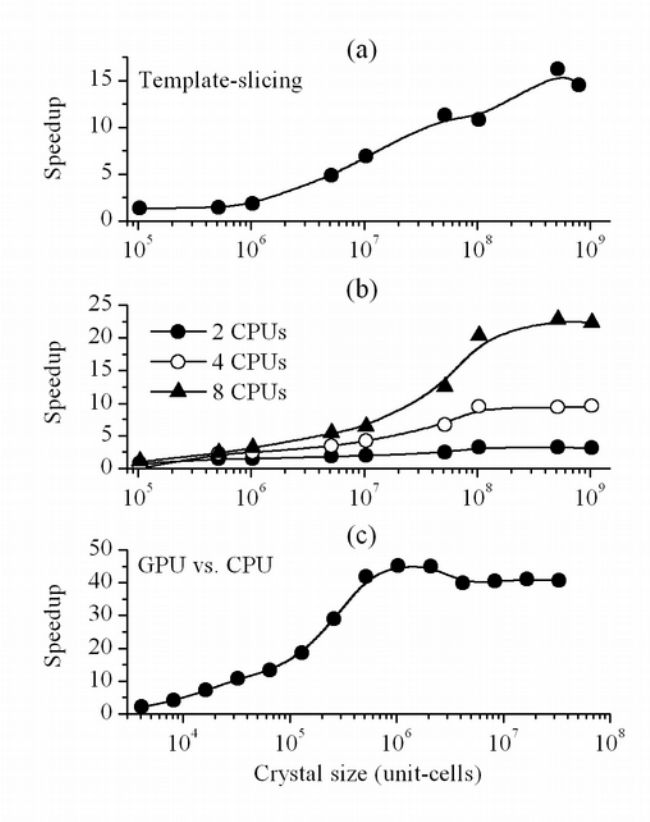

Figure 2.

(a) speedup obtained when using the template-slicing approach *vs.* the direct evaluation of equation (12) in the computation of the displacement field, equation (11).

(b) speedup obtained with the use of an increased number of CPUs in parallel, in the computation of equation (11).

(c) speedup obtained with the GPU-based computing of equations (9) and (10), *vs.* CPU computing.

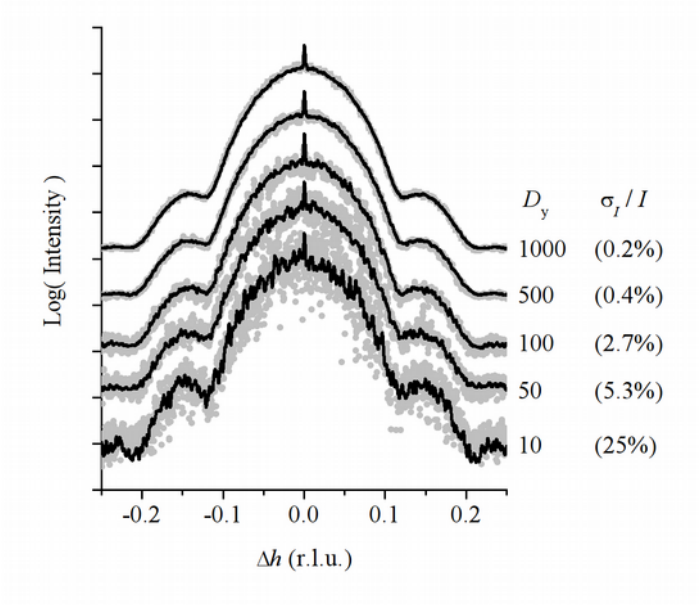

Figure 3.

Computed *h*-scans with increasing number of lattice planes in the *y*-direction, indicated at the right (the numbers in bracket indicate the relative rms deviation of the intensity, σ_I / I). Gray dots: without convolution; Black lines: with convolution. The following defects characteristics were assumed: random distribution of spherical (R_1 = 5 nm) defects with concentration $\langle c_1 \rangle = 10^{-5}$ defects / unit-cell) and lattice mismatch ε = 5%. The curves are shifted vertically for clarity.

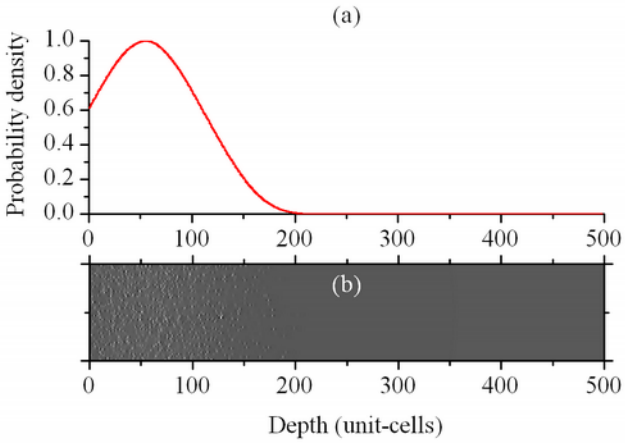

Figure 4.

(a) density function corresponding to the probability (used in the example of Sec. 4.1) of finding a defect at a given depth below the surface.

(b) 100×500 unit-cells section of a computed two-dimensional strain field. The defects are distributed according the above density function and have radius R_1 = 5 Å and mismatch ε = 5%. White: tensile strain; black: compressive strain.

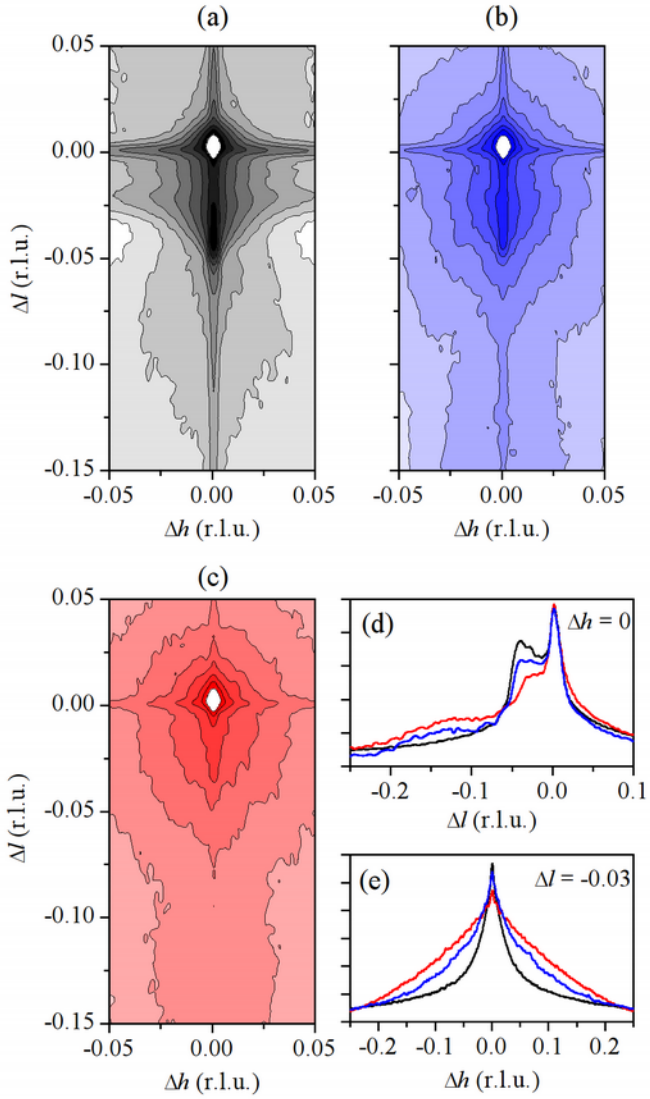

Figure 5.

Computed 004 RSMs with a non-uniform and bimodal distribution of defects (corresponding to the example used in Sec. 4.1 and Fig. 4): (a) only small defects (R_1 = 5 Å); (b) small and large (R_2 = 5 nm) defects; (c) only large defects. In all maps the logarithm of the intensity is plotted; each contour line corresponds to a $10^{0.5}$ variation. The intensity is truncated at I_{max} / 10 (white region in the center) to highlight the DXS. (d) *l* - scans extracted at $\Delta h = 0$ evidencing the damage-induced streak. (e) *h* - scans extracted at Δl = -0.03 evidencing the DXS intensity. The black, blue and red lines correspond to scans extracted from (a), (b) and (c), respectively. Each graduation corresponds to a ×10 variation.

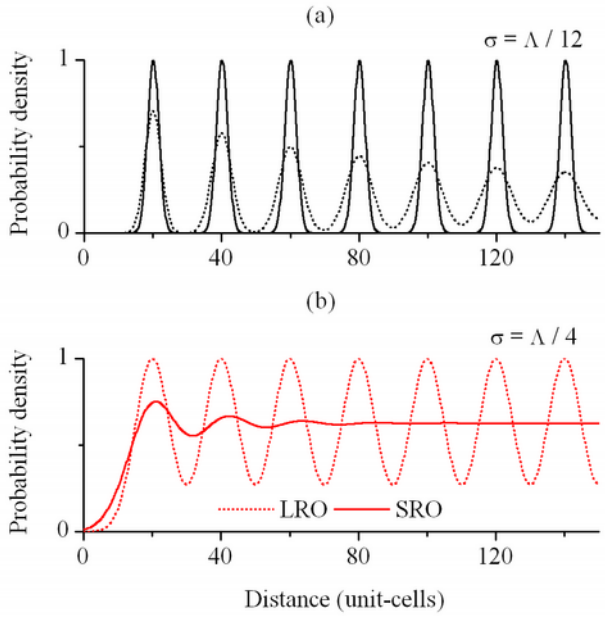

Figure 6.

Probability density function (corresponding to example of Sec. 4.2) in the case of low (a) and high (b) positional disorder, for LRO (continuous lines) and SRO (dotted lines).

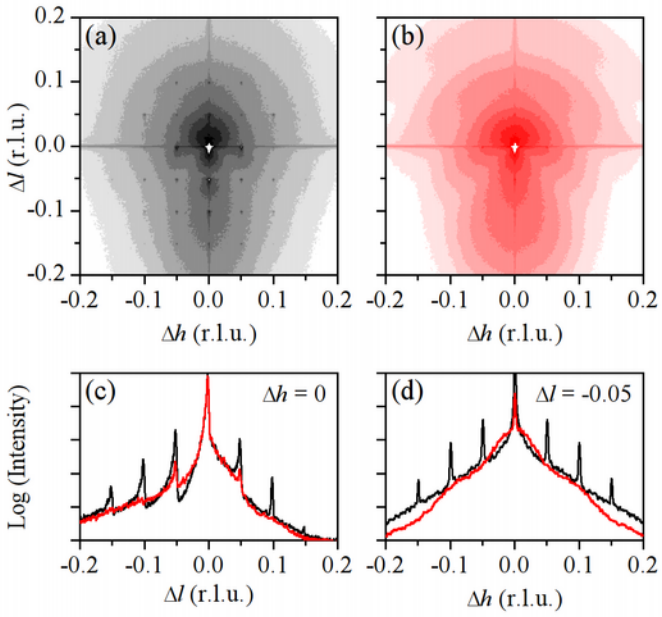

Figure 7.

Computed 004 RSMs in the case of spherical defects with LRO spatial correlations (corresponding to the example used in Sec. 4.2 and Fig. 6): (a) low positional disorder ($\sigma_0 = \Lambda /12$); (b) high positional disorder ($\sigma_0 = \Lambda /12$). In all maps the logarithm of the intensity is plotted; each contour line corresponds to a $10^{0.5}$ variation. The intensity is truncated at I_{max} / 10 (white region in the center) to highlight the DXS. (d) *l* - scans extracted at $\Delta h = 0$ evidencing the superstructure peaks. (e) *h* - scans extracted at $\Delta l = -0.05$ evidencing the DXS intensity and the superstructure peaks. The black and red lines correspond to scans extracted from (a) and (b), respectively. Each graduation corresponds to a ×10 variation.

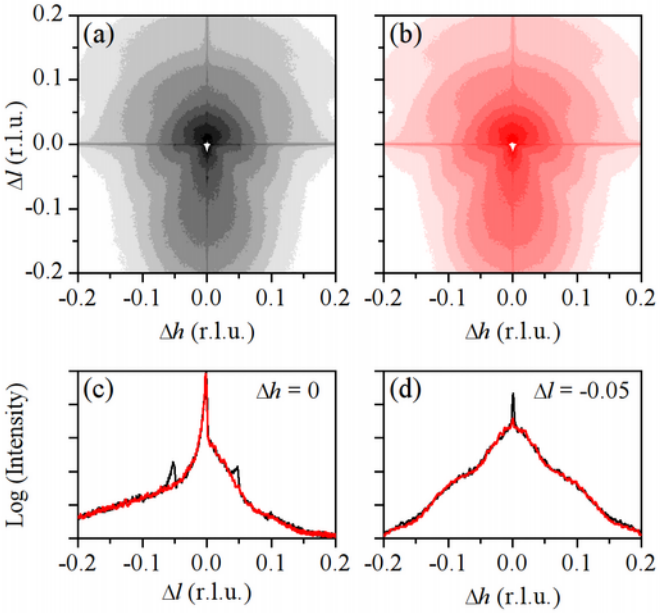

Figure 8.

Same as in Fig. 7 in the case of SRO.